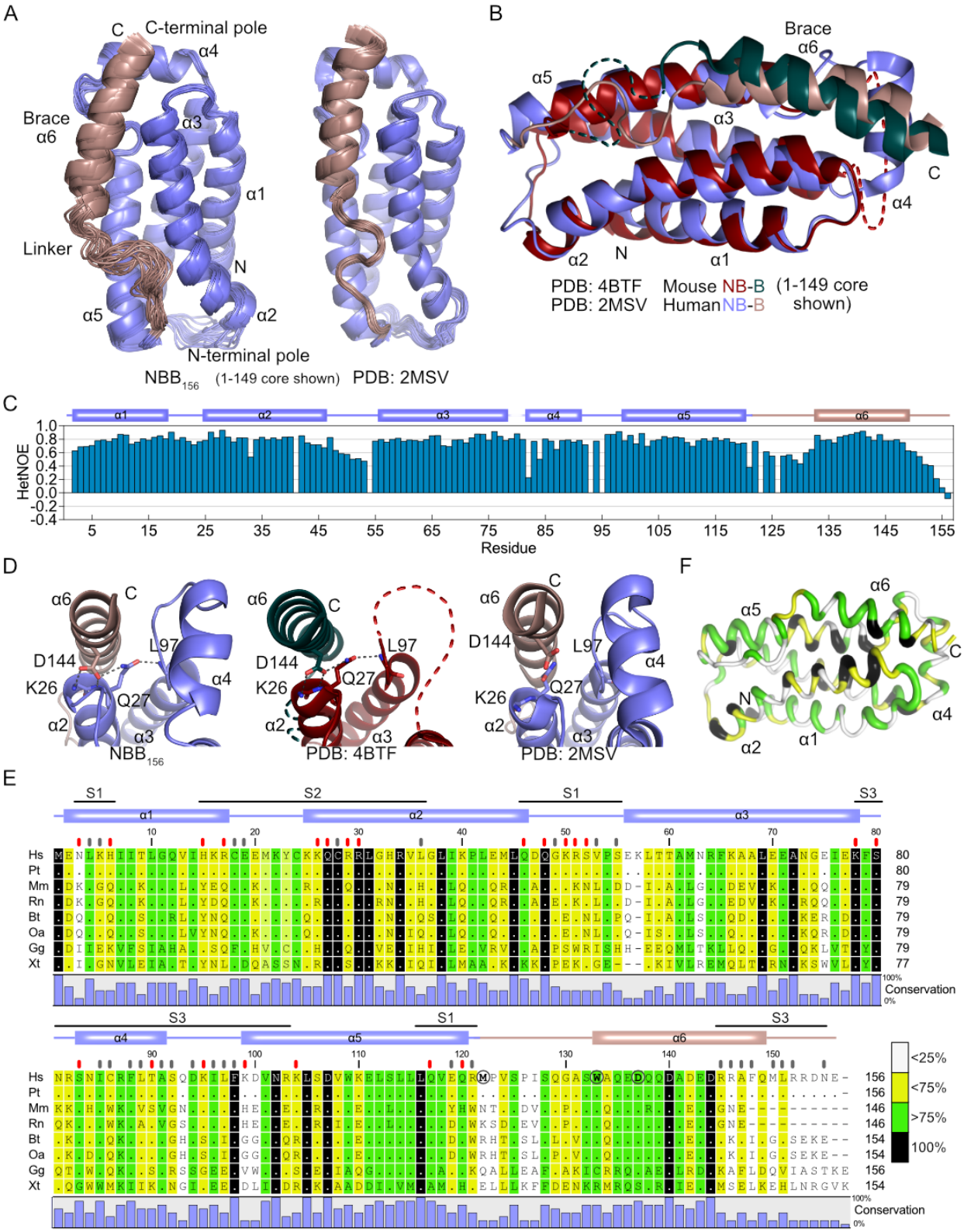

Figure S1. NMR structure of hNBB$_{156}$ reveals conservation of the auto-inhibitory mechanism. Related to Figure 1. (see legend next page)

Figure S1. NMR structure of $hNBB_{156}$ reveals conservation of the auto-inhibitory mechanism. Related to Figure 1.
A. Cartoon representation for the overlay of 20 lowest-energy conformers of $hNBB_{156}$ (PDB 6D74) and $hNBB_{2\text{-}154}$ (2MSV).
B. Cartoon representation for the overlay of human and mouse NBB structures.
C. Heteronuclear NOEs plotted per residue for NBB_{156}.
D. Zoomed-in view of the interaction between the brace helix α6 and NB for the three NBB structures.
E. Sequence alignment of NBB_{156} for *Homo sapiens* (Hs), *Pan troglodytes* (Pt), *Mus musculus* (Mm), *Rattus norvegicus* (Rn), *Bos taurus* (Bt), *Ovis aries* (Oa), *Gallus gallus* (Gg), and *Xenopus tropicalis* (Xt). Identical or similar residues of human or mouse MLKL in IP-binding sites are marked with a red vertical line symbol. These residue types coordinate IPs in other proteins. Dissimilar residues are marked with a grey symbol. Mutated sites analyzed in this study are circled.
F. Sequence conservation scaled to backbone width mapped over the tube representation of $hNBB_{156}$ structure and color-coded according to the alignment in (D).

NMR distance and dihedral constraints	hMLKL
Distance constraints	
Total number of NOEs	1749
Intramolecular	570
Short range (|i-j| ≤ 1)	418
Medium-range (1 ≤ |i-j| ≤ 5)	370
Long-range (|i-j| ≥ 5)	391
Hydrogen bonds	180
Total dihedral angle constraints	
Phi (ϕ)	127
Psi (ψ)	127
Target function	5.30 ± 0.47
Violations	
Upper Distance (max) (Å)	0.31 ± 0.08
Lower Distance (max) (Å)	0.05 ± 0.02
Angle (max) (^{o})	6.59 ± 0.86
Average pairwise r.m.s. deviation (Å)[a]	
Backbone	0.64 ± 0.11
Heavy atom	1.24 ± 0.11
Ramachandran statistics	
Residues in most favorable region (%)	95.4 %
Residues in additional favorable region (%)	4.5 %
Residues in generously allowed region (%)	0.0 %
Residues in disallowed region (%)	0.0 %

[a]Heavy atom and backbone RMSD is calculated for residues 2-118,131-150.
Abbreviations: NOE, nuclear Overhauser effect; RMSD, root mean square deviation
Table S1. Related to Figure 1. NMR structure calculation and refinement statistics for hMLKL NBB_{156}.

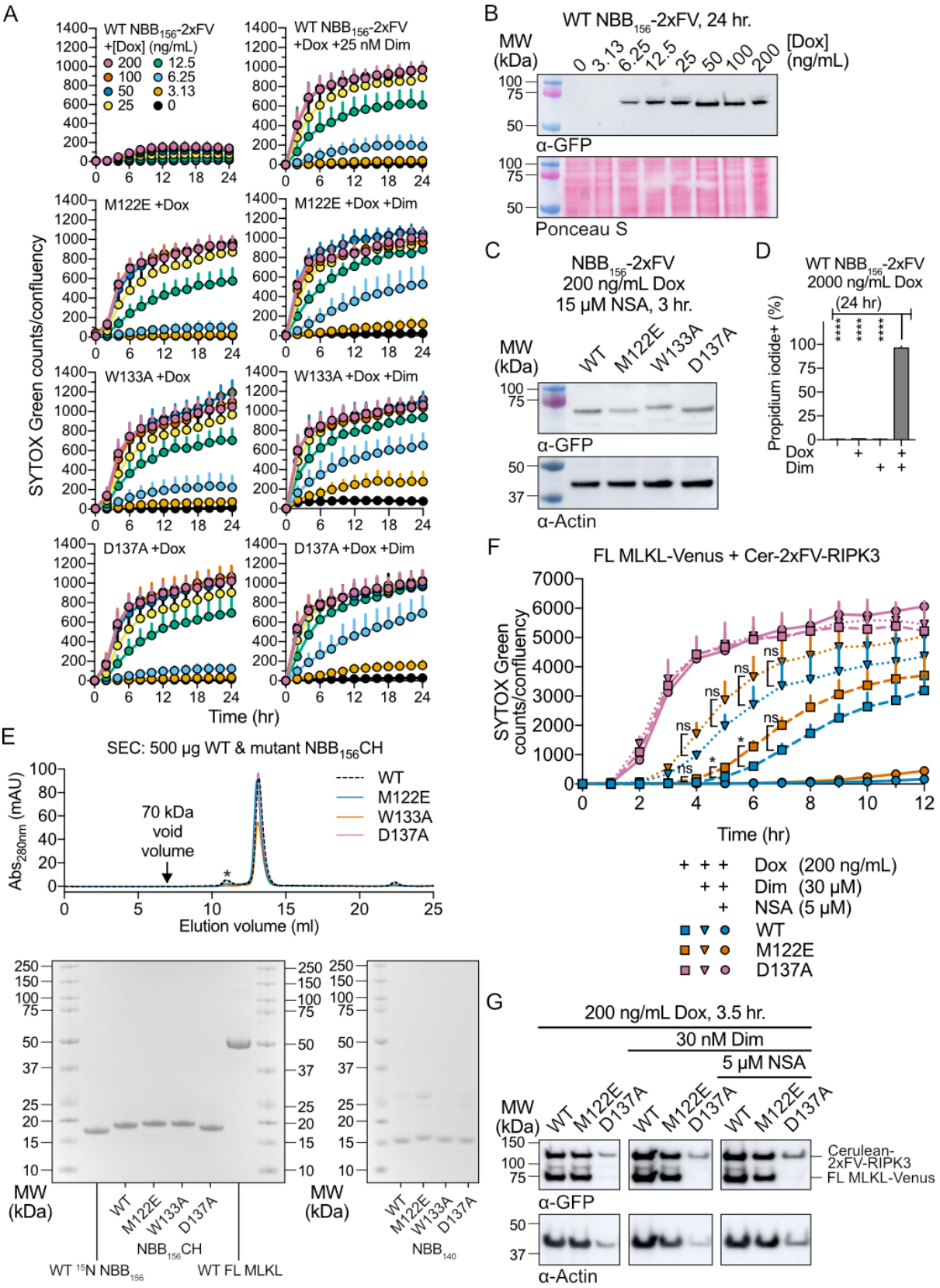

Figure S2. (see legend next page)

Figure S2. Cell death analysis reveals hyperactive NBB_{156} mutants in auto-inhibitory region. Related to Figure 1.

A. IncuCyte analysis of Dox titration examining necroptosis induced by WT and linker-brace mutants of NBB_{156} linked to two drug-inducible FKBP dimerization domains (2xF) and Venus (V) (NBB_{156}-2xFV) in *ripk3*$^{-/-}$ *mlkl*$^{-/-}$ MEFs. Error bars represent mean + SEM (n=3 independent experiments done in triplicate).

B. Western blotting for WT NBB_{156}-2xFV over indicated concentrations of Dox.

C. Western blotting for WT and hyperactive mutants of NBB_{156}-2xFV in the presence of Dox and NSA at indicated concentrations. Mutations M122E and W133A mutant consistently migrated slower during SDS-PAGE perhaps due to differential binding to SDS compared with the other proteins (see also panel S2E).

D. Quantification of propidium iodide (PI) uptake monitored by FACS at 24 h for Dox-induced WT NBB_{156}-2xFV expression in *ripk3*$^{-/-}$ *mlkl*$^{-/-}$ MEFs. Error bars represent mean + SEM (n=4 independent experiments done in triplicate).

E. Analytical size-exclusion chromatography (SEC) of recombinant NBB_{156}CH WT and mutants M122E, W133A, and D137A with equal loading and similar monomeric retention times. The asterisk denotes the presence of residual (<5%) TEV protease. SDS-PAGE analysis of recombinant proteins indicating slower migration by M122E and W133A relative to WT and D137A (see also panel S2C).

F. Necroptosis monitored by IncuCyte imaging in *ripk3*$^{-/-}$ *mlkl*$^{-/-}$ MEFs induced by WT and mutant full-length (FL) MLKL tagged with Venus expressed with Dim-induced Cerulean-2xFV-RIPK3 under the control of Dox transactivation and necrosulfonamide (NSA) inhibition. Error bars represent mean + SEM (n=2 independent experiments done in quadruplicate).

G. Western blotting for WT and mutant FL MLKL-Venus in *ripk3*$^{-/-}$ *mlkl*$^{-/-}$ MEFs expressing Cerulean-2xFV-RIPK3 in the presence of Dox, Dim, and NSA at indicated concentrations and time points. D137A mutant is not inhibited by NSA, whereas NSA blocks WT and M122E. Undetectable levels of D137A protein are capable of inducing cell death. **** P<0.0001, *** P<0.005, ** P<0.01, and * P<0.05 using one-way ANOVA with Tukey-Kramer's method for multiple comparisons (D) or unpaired, two-tailed t-test with Welch's correction for individual comparisons (F).

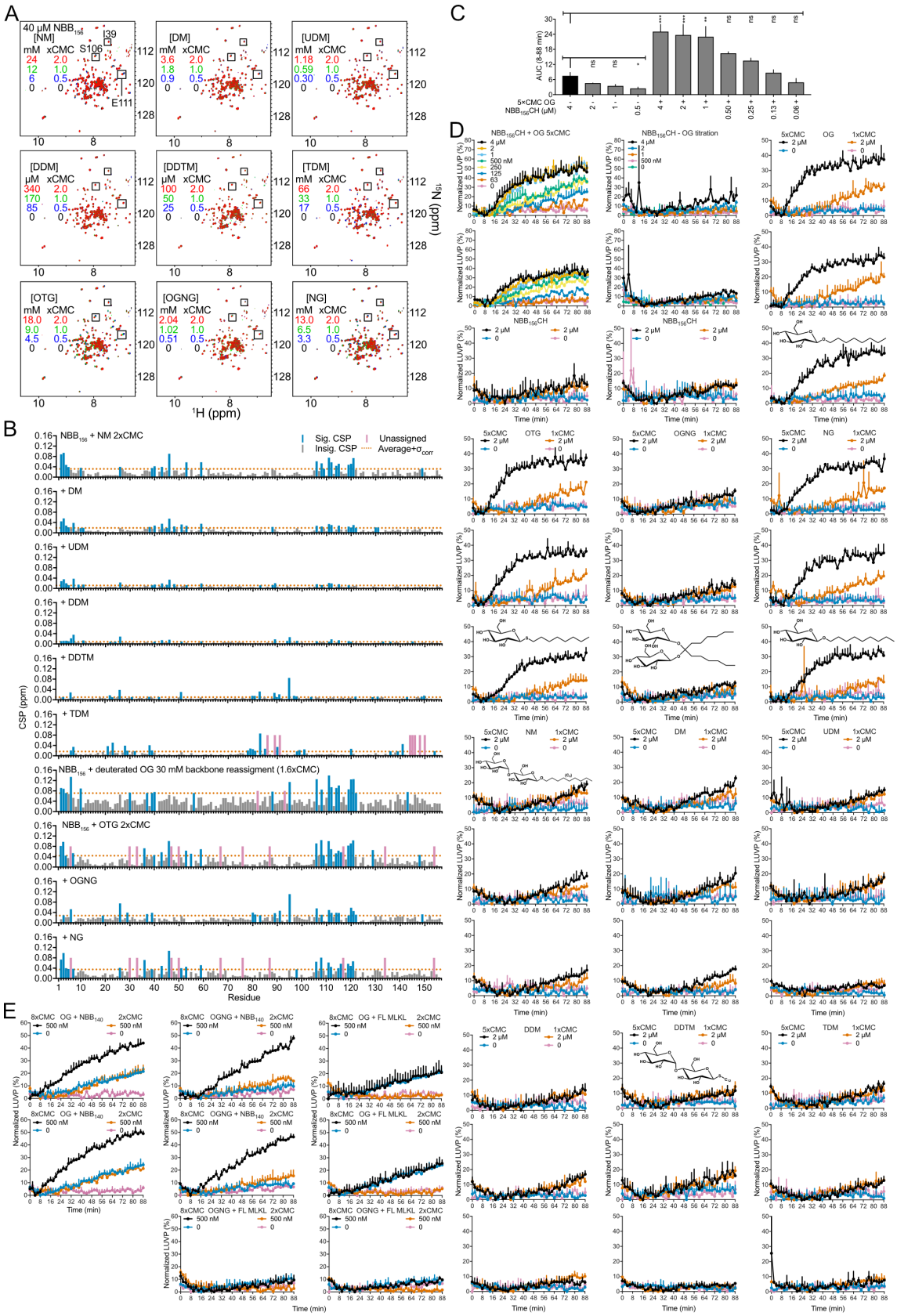

Figure S3. (see legend next page)

Figure S3. Binding-induced activation of auto-inhibited NED by glucoside detergents and IP_3. Related to Figure 2.
A. ^{15}N-^{1}H TROSY spectra of ^{15}N-NBB_{156} showing titrations up to 2×CMC for maltoside and glucoside detergents.
B. CSP analysis of data in (A) and Figure 2A. Significant (sig.) and insignificant (insig.) CSPs are colored showing residue CSPs induced in the presence of detergent with the orange dashed line marking the corrected significance cutoff (σ_{corr}) for each comparison.
C. Glucoside detergents significantly promote LUVP by AUC analysis with WT $NBB_{156}CH$ in a dose-dependent manner. Error bars represent mean + SEM (n=2 triplicate experiments).
D. Average and SD of normalized LUVP induced by $NBB_{156}CH$ in the presence of detergents used to generate related data in Figures S3C and 2E. Error bars represent mean + SD (n=3 triplicate experiments).
E. Average and SD of normalized LUVP induced by NBB_{140} and MLKL FL in the presence of detergents used to generate related data in Figures 2F and 2G. Error bars represent mean + SD (n=3 triplicate experiments).

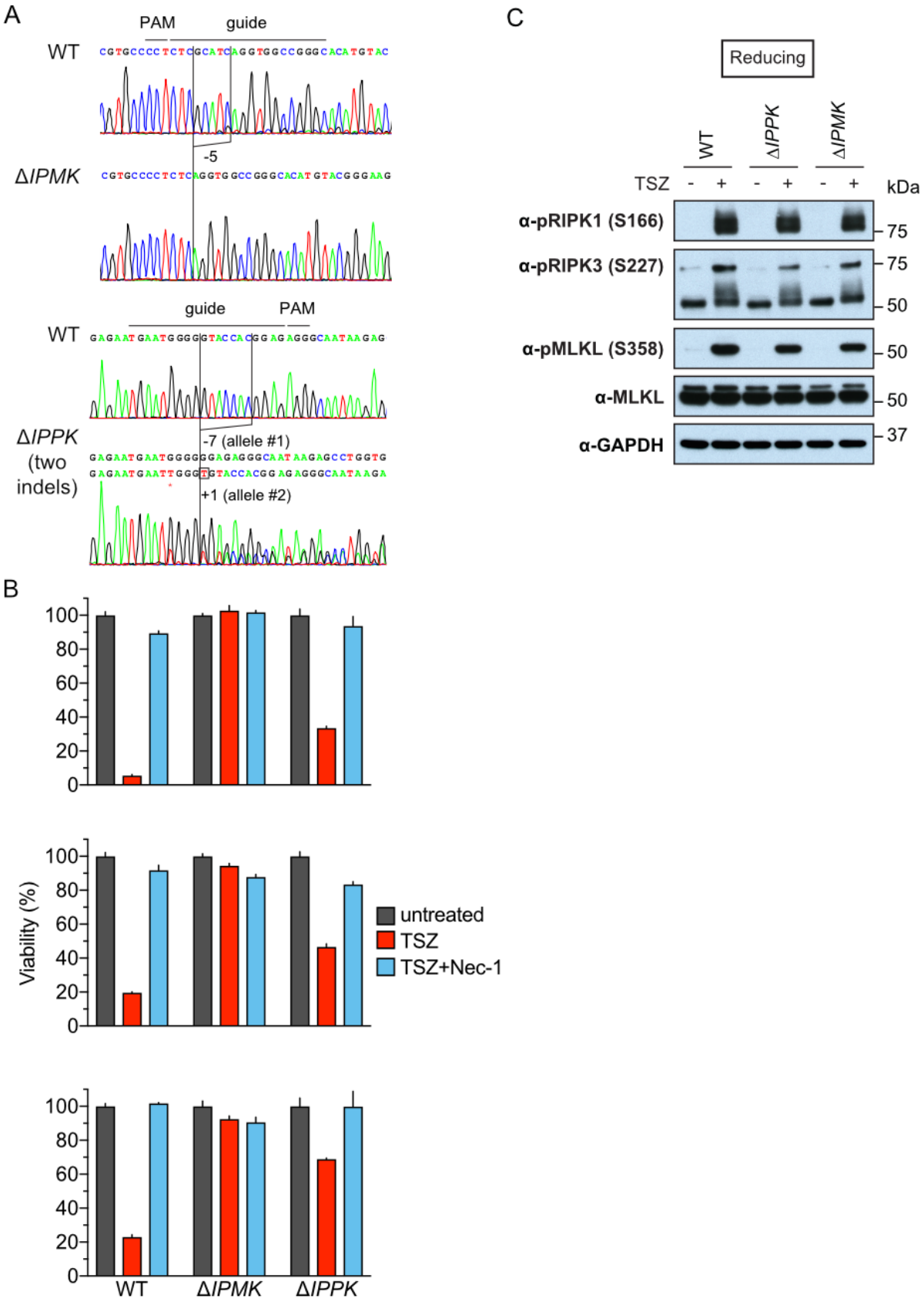

Figure S4. (see legend next page)

Figure S4. IP_6 deficiency in cells lacking IPPK contributes to necroptosis inhibition. Related to Figure 3.

A. Genomic DNAs from HT-29 clones were sequenced by PCR. The WT (upper) and deleted alleles (lower) targeted by sgRNA using CRISPR-Cas9 are shown for IPMK (top) and IPPK (bottom).

B. Independent HT-29 cell viability assays measuring cellular ATP at 24 h for WT, IPMK-deficient (Δ*IPMK*), and IPPK-deficient (Δ*IPPK*) cells in Figure 3B. Error bars represent mean + SD (n=3 triplicate experiments).

C. Western blotting of phospho-RIPK1 (S166), phospho-RIPK3 (S227), phospho-MLKL (S358), total MLKL, and GAPDH from HT-29 WT, Δ*IPMK*, and Δ*IPPK* following 6 h stimulation with TSZ to induce necroptosis.

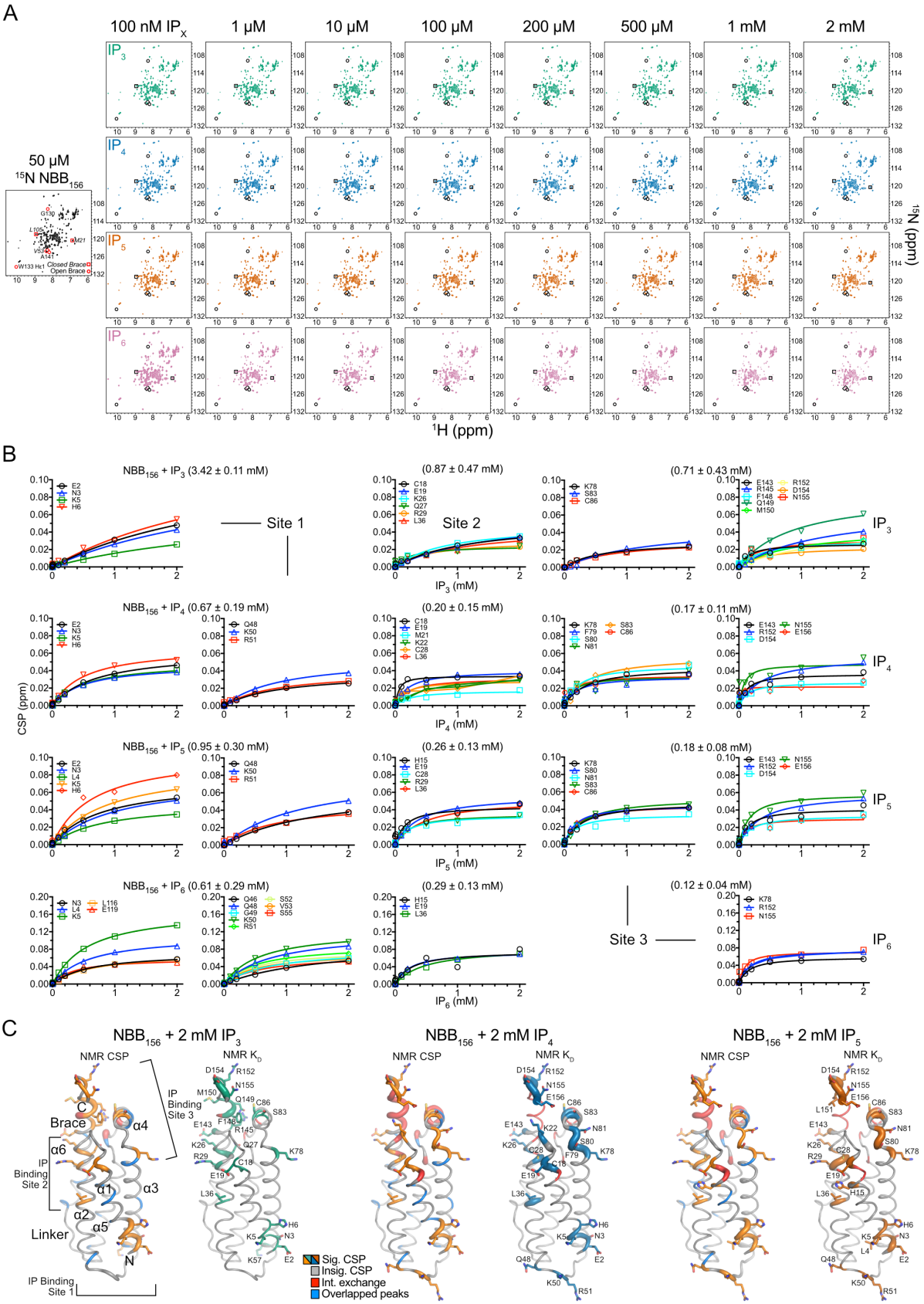

Figure S5. (see legend next page)

Figure S5. NMR CSP analysis reveals 3 independent sites for IP binding to NBB_{156}. Related to Figure 4.
A. Single ^{1}H-^{15}N SOFAST-HMQC NMR spectra of NBB_{156} in the absence (black) or presence of up to 2 mM IPs.
B. CSPs induced by IP binding to sites 1, 2, and 3 plotted as a function of IP concentration with indicated dissociation constants (K_D) from nonlinear regression.
C. CSPs were color-coded (as in Figure 4C) on indicated residues in the NBB_{156} structure putty representation with thickness of the putty proportional to the CSPs magnitude (left) or inverse NMR K_D value (right).

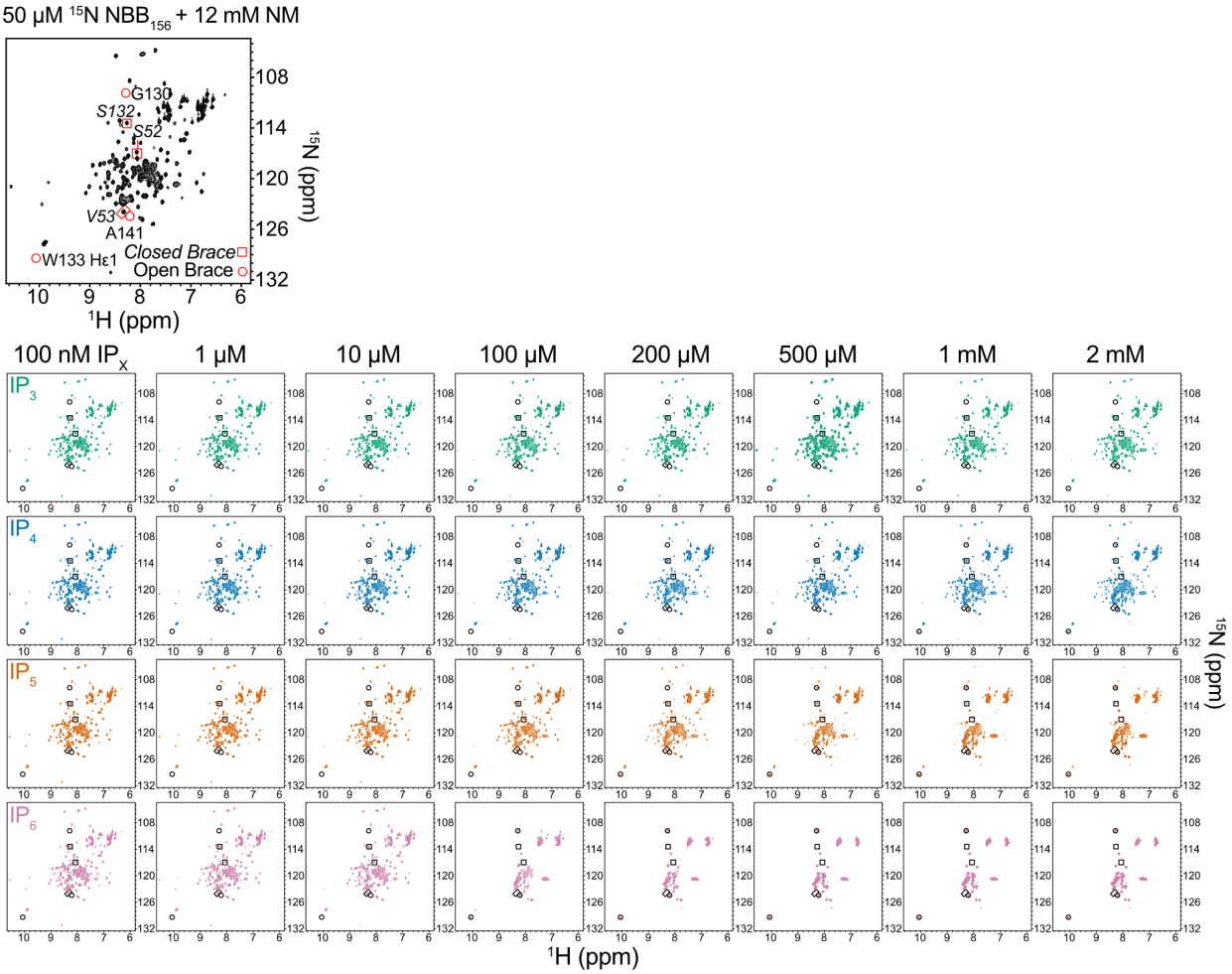

Figure S6. NMR analysis of IP binding to NBB$_{156}$ in enabling detergent supports auto-inhibited NED opening. Related to Figure 5.
Single ^{1}H-^{15}N SOFAST-HMQC NMR spectra of NBB$_{156}$ in the presence of 12 mM NM and IPs.

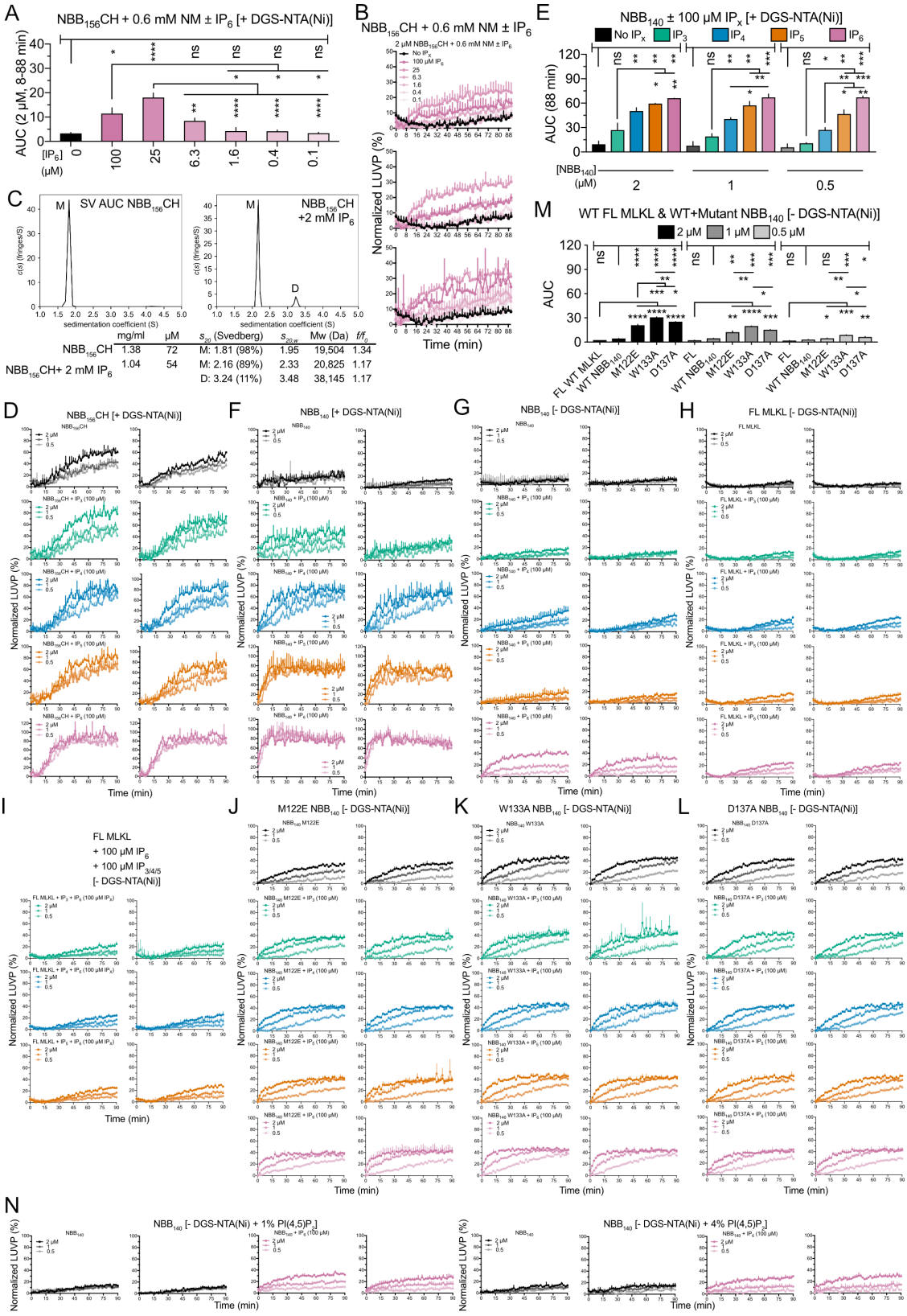

Figure S7. (see legend next page)

Figure S7. Membrane permeabilization by auto-inhibited NED and FL MLKL is promoted by IPs but not lipids. Related to Figure 6.
A. AUC analysis of LUVP for liposomes containing DGS-NTA(Ni) in the presence of $NBB_{156}CH$ preincubated in 12 mM NM (2×CMC) and up to 2 mM IP_6, before dilution 20-fold in the LUVP reaction. The final $NBB_{156}CH$ concentration was 2 μM related to data in S7B. Error bars represent mean + SEM (n=2-3 triplicate experiments).
B. Normalized LUVP by 2 μM $NBB_{156}CH$ in the presence of NM detergent and IP_6 related to data in S7A. Error bars represent mean + SD (n=3 triplicate experiments).
C. Sedimentation velocity analytical ultracentrifugation (SV AUC) of $NBB_{156}CH$ in the absence or presence of 2 mM IP_6. The sedimentation velocity profiles (fringe displacement and Rayleigh interference optical data) were fitted to a continuous sedimentation coefficient distribution model *c(s)* with sedimentation parameters tabulated for each sample.
D. Normalized LUVP by $NBB_{156}CH$ ± IPs (100 μM) in the presence of DGS-NTA(Ni).
E. AUC analysis of LUVP by NBB_{140} with liposomes containing DGS-NTA(Ni) reveals activation by 100 μM IP concentration.
F. Normalized LUVP by NBB_{140} ± IPs (100 μM) in the presence of DGS-NTA(Ni).
H. Normalized LUVP by FL MLKL ± IPs (100 μM) in the absence of DGS-NTA(Ni).
I. Normalized LUVP by FL MLKL + 100 μM IP_6 + 100 μM IP_3, IP_4, or IP_5 in the absence of DGS-NTA(Ni).
G. Normalized LUVP by WT NBB_{140} ± IPs (100 μM) in the absence of DGS-NTA(Ni).
J-L. Normalized LUVP by M122E (J), W133A (K), and D137A (L) NBB_{140} ± IPs (100 μM) in the absence of DGS-NTA(Ni).
M. AUC of LUVP for liposomes without DGS-NTA(Ni) incubated with FL MLKL and WT, M122E, W133A, and D137A NBB_{140} at different concentrations without IPs. Error bars represent mean + SEM (n=2 triplicate experiments).
N. Normalized LUVP by NBB_{140} ± IPs (100 μM) in the absence of DGS-NTA(Ni) ± $PI(4,5)P_2$.